Supplementary Information: Single photon reflection from a quantum dot in a waveguide

Tarun Patel[1], Matteo Pennacchietti[1], Sayan Gangopadhyay[2], Philip J. Poole[3], Dan Dalacu[3,4], Stephen Hughes[4] and Michael E. Reimer[1,2]

[1]Institute for Quantum Computing and Department of Electrical and Computer Engineering, University of Waterloo, Waterloo, Ontario N2L 3G1, Canada
[2]Institute for Quantum Computing and Department of Physics and Astronomy, University of Waterloo, Waterloo, Ontario N2L 3G1, Canada
[3]National Research Council of Canada, Ottawa, Ontario K1A 0R6, Canada
[4]Department of Physics, Engineering Physics and Astronomy, Queens University, Kingston, K7L 3N6, Ontario, Canada.

Supplementary Note 1 Theoretical Model

S1.1 Quantum Master Equation Model

We model the evolution of the quantum dot as a coherently driven two-level system embedded in a single mode waveguide with the following master equation:

$$\dot{\rho} = -\frac{i}{\hbar}[H_S, \rho] + \frac{\gamma}{2}\mathcal{L}[\sigma_-]\rho + \frac{\gamma'}{2}\mathcal{L}[\sigma^{11}]\rho\,, \tag{S1}$$

with the atom-field Hamiltonian

$$H_S = \hbar\Delta_{0L}\sigma^+\sigma^- + \hbar\frac{\Omega}{2}(\sigma^+ + \sigma^-)\,, \tag{S2}$$

where $\gamma = \gamma_{wg} + \gamma_0$ is the radiative decay rate of the QD into the HE_{11} waveguide mode and non-waveguide modes, respectively. Also, $\sigma^+ = |e\rangle\langle g|$, $\sigma_{ee} = \sigma^+\sigma^- = |e\rangle\langle e|$, $\Delta_{0L} = \omega_0 - \omega_L$, and $\mathcal{L}[A]\rho = 2A\rho A^\dagger - A^\dagger A\rho - \rho A^\dagger A$. The β-factor relates to the measured radiative decay rate into the waveguide mode and non-waveguide modes $\beta = \gamma_{wg}/(\gamma_{wg} + \gamma_0)$, where $T_1 = 1/\gamma_{wg}$. We estimate $\beta = 90\%$ by matching FDTD simulation results with the measured dimensions of the nanowire waveguide from SEM images.

We are working in the interaction picture in a rotating frame at the CW laser frequency ω_L, and Ω is the CW Rabi frequency, which we treat as a classical field interaction. To model the interaction of the QD with the waveguide mode, we use the standard Input-Output formalism [1] to relate the output field operators to the input field and the QD operators. We will use the labels R and T for reflection and transmission, respectively. Since the drive field Ω is travelling into the transmission port, the reflection port consists only of QD emission. Thus, we have [2],

$$a_T(t) = \sqrt{\bar{n}} - i\sqrt{\frac{\gamma_{wg}}{2}}\,\sigma^-(t)\,, \tag{S3}$$

$$a_R(t) = -i\sqrt{\frac{\gamma_{wg}}{2}}\,\sigma^-(t)\,. \tag{S4}$$

We consider the monochromatic CW drive as a coherent state $|\alpha\rangle$ such that in the rotating frame we can convert the input field operator a_{in} to simply the coherent state amplitude: $a_{in} \to \langle a_{in}\rangle = \sqrt{\bar{n}}$ where $\bar{n}$ is the mean photon number (photon flux) of the coherent state [2, 3]. In the experiment, we used the metric mean photon per lifetime $\mu = \bar{n}/T_1 = \bar{n}\gamma$, which is measured before the light is coupled to the nanowire with efficiency η_{in}. We can relate the amplitude of input coherent state to the Rabi frequency $\Omega/2 = -i\sqrt{\gamma/2}a_{in} \implies \Omega/2 = \gamma_{wg}\sqrt{\eta_{in}\mu/2}$ (neglecting phases) [2, 4]. As a result, we get the following relationship between the Rabi frequency and the input mean photon number per lifetime: $\Omega = \gamma_{wg}\sqrt{2\eta_{in}\mu}$.

S1.1.1 Reflected Intensity

We define the measured reflected photoluminescence intensity as given by the steady state expectation value of the reflected mode population, which according to S4 is directly proportional to the population of the QD,

$$I_R = \eta_{coll} \cdot \eta_{qe} \cdot \langle a_R^\dagger a_R \rangle_{ss} = \eta_{coll} \cdot \eta_{qe} \cdot \frac{\gamma_{wg}}{2} \cdot \rho_{11}^{ss} \tag{S5}$$

where η_{coll} and η_{qe} are the total photon collection efficiency and quantum efficiency of the quantum dot, respectively. The latter is simply the on-off ratio due to blinking (see Figure S9). For any operator $\dot{O}$, the equations of motion can be derived from $\langle \dot{O} \rangle = \langle \dot{\rho} O \rangle$. Defining $\rho_+ = \langle \sigma^+ \rangle$ and $\rho_{11} = \langle \sigma_{ee} \rangle$, then using Eq. S1 we obtain

$$\dot{\rho}_+ = \langle g|\dot{\rho}|e\rangle = i\Delta_{0L}\rho_+ - \frac{i\Omega}{2}(2\rho_{11} - 1) - \frac{(\gamma + \gamma')}{2}\rho_+ \,, \tag{S6}$$

and

$$\dot{\rho}_{11} = \langle e|\dot{\rho}|e\rangle = -\frac{i\Omega}{2}(\rho_+ - \rho_+^*) - \rho_{11}\gamma \,. \tag{S7}$$

In steady-state ($\dot{\rho} = 0$) these two coupled equations can be solved to produce

$$\langle \sigma_{ee} \rangle_{ss} = \rho_{11}^{ss} = \frac{\frac{\Omega^2}{4\gamma}(\gamma + \gamma')}{\frac{1}{4}(\gamma + \gamma')^2 + \Delta_{0L}^2 + \frac{\Omega^2}{2\gamma}(\gamma + \gamma')} \,. \tag{S8}$$

To model the impact of the stray background laser in the detected signal, we add a fraction of coherent light to the output signal as $I_{bg} = \eta_{coll} \cdot b_{frac} \cdot A_{in}$ where $A_{in} = \langle a_{in} \rangle^2 = \eta_{in} \cdot \mu$. To model the spectral diffusion caused by charge noise, we numerically convolve I_R with a normalized Gaussian as a function of detuning Δ. As a result, the total measured fluorescence as a function of Ω and Δ is

$$I_{meas}(\Omega, \Delta) = \eta_{coll}\eta_{qe}\frac{\gamma_{wg}}{2}\int_{-\infty}^{\infty} \rho_{11}^{ss}(\Omega, \Delta - \delta)\,\frac{e^{-\frac{\delta^2}{2\sigma^2}}}{\sqrt{2\pi}\sigma} d\delta + \eta_{coll} b_{frac} A_{in}. \tag{S9}$$

We can estimate b_{frac} via the count rate when off resonance with the QD (i.e. when $\Delta \gg \gamma, \gamma'$ then $\rho_{11}^{ss} = 0$). To generate the model curve in Figure 3a of the main text, we first fit a normalized Voigt function to the raw data and extract the Gaussian linewidth contribution σ (standard deviation), the total Lorentzian linewidth (half-width at half-maximum) $\gamma_L = (\gamma + \gamma')/2$ and estimate b_{frac} from the vertical offset obtained from the fit. In the case of Figure 3a of the main text, the Voigt

fit returned $\sigma = 1.9 \pm 0.3$ GHz and $\gamma_L = 0.6 \pm 0.4$ GHz. Next, to generate the model curve, we pass the parameters from the Voigt fit (pure dephasing γ', inhomogeneous broadening σ and b_{frac}) to Eq. S9 where we implement a numerical convolution of ρ_{11}^{ss} with a Gaussian. We let μ be the only free parameter and all other parameters are fixed as: $\eta_{in} = 0.85, \beta = 0.9, \eta_{col} = 0.5, \eta_{QE} = 0.95, 1/\gamma_{wg} = 894$ ps (see Supplementary Note 4 for how these parameters are calculated/estimated).

To generate the model curve in Figure 3b of the main text, we numerically integrate over the modeled response shown in Figure 3a and plot the fraction $(\int I_{meas}(\Omega, \Delta) d\Delta - I_{bg})/I_{gb}$ as R_{int}. R_{int} is then plotted for μ ranging from 1E^{-6} to 1E^{3}. The remaining parameters were fixed to the same values used in the fit of Figure 3a of the main text (see Supplementary Note 4). To generate the data points in Figure 3b, we assume that $\sigma > \gamma + \gamma'$ (lineshape is dominated by a Gaussian), and fit the data to a Gaussian: $A \exp\left(-\frac{\delta^2}{2\sigma^2}\right)/\sqrt{2\pi} + b$. Then, the total reflected intensity ("area under the curve") of each scan is $R_{int-data} = A\sigma/b$.

S1.1.2 Coherent and Incoherent Contribution

It is useful to separate out the coherent and incoherent contributions of the emission. The fluctuation operator of the TLS is defined from

$$\sigma_\delta^- = \sigma^- - \langle \sigma^- \rangle , \tag{S10}$$

$$\sigma_\delta^+ = \sigma^+ - \langle \sigma^+ \rangle . \tag{S11}$$

If we consider the resonant case, ($\Delta_{0L} = 0$), and the total intensity from the TLS is

$$I_{\text{tot}} = I_{\text{coh}} + I_{\text{inc}}, \tag{S12}$$

where we derive

$$I_{\text{coh}} = \langle \sigma^+ \rangle_{\text{ss}} \langle \sigma^- \rangle_{\text{ss}} = \rho_+(t_{\text{ss}}) \rho_-(t_{\text{ss}}) = \frac{1}{2} \frac{\frac{2\Omega^2}{(\gamma+\gamma')^2}}{\left(1 + \frac{2\Omega^2}{\gamma(\gamma+\gamma')}\right)^2}, \tag{S13}$$

and

$$I_{\text{inc}} = \langle \sigma_\delta^+ \sigma_\delta^- \rangle_{\text{ss}} = I_{\text{tot}} - I_{\text{inc}} = \sigma_{11}(t_{\text{ss}}) - |\rho_+(t_{\text{ss}})|^2 = \frac{1}{2} \frac{\frac{2\Omega^2}{\gamma(\gamma+\gamma')} \left(\frac{1}{\gamma} - \frac{1}{\gamma+\gamma'}\right) + \frac{4\Omega^4}{\gamma^2(\gamma+\gamma')^2}}{\left(1 + \frac{2\Omega^2}{\gamma(\gamma+\gamma')}\right)^2}. \tag{S14}$$

In the limit that $\gamma' = 0$, we recover the standard result (equations 2.125 and 2.126 in Ref. [5]), which implies the following:

1. Neglecting pure dephasing, the ratio of incoherent to coherent is simply
$$\frac{I_{\text{inc}}}{I_{\text{coh}}} = \frac{2\Omega^2}{\gamma^2} . \tag{S15}$$
2. At low Rabi field ($\Omega \ll \gamma, \gamma'$), coherent scattering with the linewidth of the narrow drive laser dominates, as expected from perturbation theory.
3. At larger Rabi fields ($\Omega > \gamma, \gamma'$), the incoherent scattering dominates, and in this regime, we observe spectral signatures of Mollow sidebands, which can also be probed through the reflection port.

S1.1.3 Second Order Correlation of Reflected Intensity

To compute the second order correlation function for $G^{(2)}(\tau) = \langle \sigma^+(t_{\rm ss})\sigma^+(t_{\rm ss},\tau)\sigma^-(t_{\rm ss},\tau)\sigma^-(t_{\rm ss})\rangle$ we can derive equations for

$$\frac{d}{d\tau}\langle \sigma^+(t_{\rm ss})\sigma^+(t_{\rm ss}+\tau)\sigma^-(t_{\rm ss}+\tau)\sigma^-(t_{\rm ss})\rangle = \frac{d}{d\tau}h(\tau) \tag{S16}$$

and

$$\frac{d}{d\tau}\langle \sigma^+(t_{\rm ss})\sigma^+(t_{\rm ss}+\tau)\sigma^-(t_{\rm ss})\rangle = \frac{d}{d\tau}f(\tau) \tag{S17}$$

Since the left (σ^+) and right (σ^-) operators are evaluated in the steady state, they are independent of τ and we only need to focus on the operators that depend on τ. Therefore, we effectively have equations of motion for $\sigma_{ee}(\tau)$ and $\sigma_+(\tau)$, i.e. ρ_{11} and ρ_+, respectively. Indeed, we define $h(\tau) = \rho_{++--}(\tau)$ and $f(\tau) = \rho_{++-}(\tau)$ as the new density operators with the respective operator terms in the subscript. Now, we can use the two solutions for the one-time equations of motion Eq. S7 and Eq. S6 for $\frac{d}{d\tau}h(\tau)$ and $\frac{d}{d\tau}f(\tau)$, respectively, where we instead differentiate with respect to time τ. We will use Laplace transforms to obtain an algebraic solution from the differential equations Eq. S7 and Eq. S6 and perform an inverse Laplace transform for the main $G^{(2)}(\tau)$ of interest. In Laplace space we have

$$sH(s) - h(0) = -\frac{i\Omega}{2}(F(s) - F^*(s)) - H(s)\gamma \tag{S18}$$

and

$$sF(s) - f(0) = -\frac{i\Omega}{2}\left(2H(s) - 1/s\right) - \left(\frac{\gamma+\gamma'}{2} - i\Delta\right)F(s), \tag{S19}$$

and similarly,

$$sF^*(s) - f^*(0) = \frac{i\Omega}{2}\left(2H(s) - 1/s\right) - \left(\frac{\gamma+\gamma'}{2} + i\Delta\right)F^*(s), \tag{S20}$$

and these can be solved algebraically. The inverse Laplace transfrom of $H(s)$ gives the required solution, namely $h(\tau) = G^{(2)}(\tau)$, in reflection. The general analytical solution in Laplace space is

$$F(s) \equiv \frac{2H(s)}{\Omega^2} = \frac{\left(s + \frac{\gamma+\gamma'}{2}\right)}{s(s+\gamma)\left(s^2 + (\gamma+\gamma')^2/4 + s^2(\gamma+\gamma') + \Delta^2\right) + s\Omega^2(s + \frac{\gamma+\gamma'}{2})}, \tag{S21}$$

and $G^{(2)}(\tau)$ is obtained from an Inverse Laplace Transform:

$$f(\tau) \equiv \frac{2G^{(2)}(\tau)}{\Omega^2} = \mathcal{L}^{-1}[F(s)](\tau) = \int_{c-i\infty}^{c+i\infty} ds\, e^{s\tau}F(s)\,. \tag{S22}$$

Then, we define $g^{(2)}(\tau) = G^{(2)}(\tau)/G^{(2)}(\tau \to \infty)$.

Influence of Spectral Diffusion. The effect of spectral diffusion on the autocorrelation function is similar to that of pure dephasing, it leads to a narrowing of the anti-bunching dip at $\tau = 0$. We have derived the correlation function $\bar{g}^{(2)}(\tau, \Delta, \Omega)$ that has the detuning included. Next, we take an average for many different detunings Δ_i that are sampled smoothly and evenly from a Gaussian

distribution. This outputs a set of correlation functions $g_i^{(2)}(\tau, \Delta_i, \Omega)$, which are all normalized to 1 for $\tau \to \infty$. Now, the normalized nature of the correlation function is important to take into account when performing the averaging. The Gaussian sampling of the detunings ensures that the number of correlation functions at a given detuning is representative of the experiment; however, it does not take into account the probability of detection of this version of $g^{(2)}(\tau, \Omega, \Delta_i)$ in the experiment. To include this, we must perform a weighted average using the steady state atomic expectation value at Ω and Δ as the weights. Since there are two detectors in the HBT experiment, we take the square of the steady state atomic expectation value.

$$\bar{g}^{(2)}(\tau, \Omega) = \sum_i^N \frac{1}{N} \frac{\langle \rho_{11}(\Omega, \Delta_i) \rangle_{ss}^2}{4} g_i^{(2)}(\tau, \Delta_i, \Omega). \tag{S23}$$

Impact of Blinking and the Background Laser to the Autocorrelation Function. We model blinking using the function and parameters determined in Figure S9. To model the impact of the background laser, we add a constant to $g^{(2)}(\tau)$ proportional to the amount of detected background, since for a coherent state $g^{(2)}(\tau) = 1$. Thus, $g^{(2)}(0) = I_{bg}/I_{meas} = p_{floor}$, i.e., it is the background collected as a fraction of the total intensity when performing HBT

$$g^{(2)}(\tau) = \bar{g}^{(2)}(\tau)\, g^{(2)}_{blink}(\tau)\, (1 - p_{floor}) + p_{floor}\,. \tag{S24}$$

Fast Numerical Implementation of Laplace Inversions

We begin with the Laplace-domain function

$$F(s) = \frac{s + \frac{(\gamma+\gamma')}{2}}{s\left[(s+\gamma)\left(s^2 + \frac{(\gamma+\gamma')^2}{4} + s(\gamma+\gamma') + \Delta^2\right) + \Omega^2(s + \frac{(\gamma+\gamma')}{2})\right]}\,.$$

Expanding the denominator,

$$F(s) = \frac{s + \frac{(\gamma+\gamma')}{2}}{sD(s)},$$

where the cubic polynomial

$$D(s) = s^3 + As^2 + Bs + C,$$

and A, B, C collect the coefficients from the expansion above.

$$\begin{aligned} A &= 2\gamma + \gamma'\,, \\ B &= \frac{(\gamma+\gamma')^2}{4} + \Delta^2 + \gamma(\gamma+\gamma') + \Omega^2\,, \\ C &= \gamma\frac{(\gamma+\gamma')^2}{4} + \gamma\Delta^2 + \Omega^2\frac{(\gamma+\gamma')}{2}\,. \end{aligned}$$

Poles and Residues. The poles of $F(s)$ occur at $s = 0, p_1, p_2, p_3$, where p_k are the roots of $D(s)$. Assuming $C \neq 0$ and that all poles are simple, we compute the residues at these poles.

Residue at $s = 0$:

$$\mathrm{Res}(F, 0) = \lim_{s\to 0} sF(s) = \lim_{s\to 0} \frac{s + \frac{(\gamma+\gamma')}{2}}{sD(s)} = \frac{\frac{(\gamma+\gamma')}{2}}{C}.$$

Residue at $s = p_k$:

$$\begin{aligned}\mathrm{Res}(F, p_k) &= \lim_{s\to p_k} (s - p_k)F(s) = \lim_{s\to p_k} \frac{(s - p_k)(s + \frac{(\gamma+\gamma')}{2})}{sD(s)} \\ &= \frac{p_k + \frac{(\gamma+\gamma')}{2}}{p_k D'(p_k)}.\end{aligned}$$

Partial fraction expansion. For a rational function $F(s) = \frac{b(s)}{a(s)} = \frac{\sum_{k=0}^{n} b_k s^k}{\sum_{l=0}^{m} a_l s^l}$ where $(n, m) > 0$, the general partial fraction expansion reads

$$F(s) = \frac{r_m}{s - p_m} + \frac{r_{m-1}}{s - p_{m-1}} + \cdots + \frac{r_0}{s - p_0} + k(s),$$

where $r_m, \ldots, r_1$ are the residues of $F(s)$ and $k(s) = 0$ since the fraction is proper.

Therefore, in our case,

$$F(s) = \sum_{k=1}^{3} \frac{p_k + \frac{(\gamma+\gamma')}{2}}{p_k D'(p_k)} \cdot \frac{1}{s - p_k} + \frac{\frac{(\gamma+\gamma')}{2}}{Cs}.$$

Inverse Laplace transform.

Using

$$\mathcal{L}^{-1}\left\{\frac{1}{s}\right\} = 1, \quad \mathcal{L}^{-1}\left\{\frac{1}{s - p_k}\right\} = e^{p_k t},$$

we obtain

$$\mathcal{L}^{-1}\{F(s)\}(t) = \frac{\frac{(\gamma+\gamma')}{2}}{C} + \sum_{k=1}^{3} \frac{p_k + \frac{(\gamma+\gamma')}{2}}{p_k D'(p_k)} e^{p_k t}.$$

The only numerical step is to compute the p_k, i.e., the roots of the polynomial.

S1.1.4 Squeezing Spectrum

Let us introduce the general squeezing operator along a given quadrature angle of ϕ,

$$X^{\phi} = \frac{1}{2}(e^{i\phi}\sigma^{+} + e^{-i\phi}\sigma^{-}), \tag{S25}$$

and which implies the fluctuation operator is

$$X_{\delta}^{\phi} = \frac{1}{2}(e^{i\phi}\sigma_{\delta}^{+} + e^{-i\phi}\sigma_{\delta}^{-})\,. \tag{S26}$$

The squeezing (stationary) spectrum is obtained from the equation [6, 7]

$$S(\omega,\theta) \equiv 4\mathrm{Re}\int_{-\infty}^{\infty} d\tau e^{i(\omega-\omega_L)\tau}\; T\left\langle :X_\delta^\phi(t_{\mathrm{ss}})X_\delta^\phi(t_{\mathrm{ss}}+\tau):\right\rangle, \tag{S27}$$

where and the operation T applies the correct ordering of time, with normally ordered products; thus $\sigma^-(t+\tau)$ is to the left of $\sigma^-(t)$, while $\sigma^+(t+\tau)$ is to the right of $\sigma^+(t)$. Expanding the integrand

$$4\left\langle :X_\delta^\phi(t_{\mathrm{ss}})X_\delta^\phi(t_{\mathrm{ss}}+\tau):\right\rangle =$$
$$\left\langle\sigma^+(t_{\mathrm{ss}})\sigma^-(t_{\mathrm{ss}}+\tau)\right\rangle + \left\langle\sigma^+(t_{\mathrm{ss}}+\tau)\sigma^-(t_{\mathrm{ss}})\right\rangle \tag{S28}$$
$$+e^{2i\theta}\left\langle\sigma^+(t_{ss})\sigma^+(t_{\mathrm{ss}}+\tau)\right\rangle + e^{-2i\theta}\left\langle\sigma^-(t_{\mathrm{ss}}+\tau)\sigma^-(t_{\mathrm{ss}})\right\rangle, \tag{S29}$$

we find that there are four two-time correlation terms that must be computed. We compute these terms using QuTiP with the Hamiltonian in Eq. S2 [8]. It is important to note that the signature of squeezing from Eq. S25 is a minimum negative value at some θ and some positive maximum value at $\theta+\pi/2$ [7]. In other words, the prescence of a negative value of $S(\theta,\omega)$ indicates there is quadrature squeezing in the florescence. In Figure S1 we show two examples of the normalized squeezing spectrum $S(\theta,\omega)$, one with no pure dephasing of the TLS ($\gamma'=0$) and one with pure dephasing ($\gamma'=\gamma$). As expected, in the absence of pure dephasing, at $\omega=0$ we see the minimum value of -1 at $\theta=\pi/2$ and the maximum value at $\theta=0,\pi$, indicating that there is significant squeezing of the quadrature within the incoherent component of the fluorescence. However, when a significant but experimentally plausible level of pure dephasing is included, the negativity in the plot disappears, signifying that there is no squeezing present. Interestingly , we still observe a significant anti-bunching dip at $\tau=0$ in the HBT autocorrelation histogram even in the presence of finite pure dephasing values, as evidenced by Figure 4a of the main text. Indeed, the resonance fluorescence of a single two-level system will always exhibit anti-bunching [9]. This suggests that although quadrature squeezing and anti-bunching may arise together, as in the case of no dephasing, it is possible to observe anti-bunching but not quadrature squeezing. In other words, squeezing does not imply anti-bunching, just as anti-bunching does not imply sub-Poissonian counting statistics [9]. Instead, anti-bunching is the result of the discrete nature of the two-level system exchanging single quanta of energy with over its radiative lifetime [10].

S1.2 Quantum Trajectory Model

For generating quantum trajectories, we followed closely Ref [2]. We utilized the same Hamiltonian in Eq. S1 and set $\Delta=0$. We also set $\beta=1 \implies \gamma=\gamma_{wg}$ and remove any pure dephasing ($\Gamma'=0$). Rather than setting γ_{wg} to be the trajectory collapse operator, we can use Eq S4 to define two collapse operators that describe the emission of photons into either the reflection or transmission port:

$$C_R^- = ia_R = \sqrt{\frac{\gamma_{wg}}{2}}\,\sigma^-(t), \tag{S30}$$
$$C_T^- = ia_T = \sqrt{\frac{\gamma_{wg}}{2}}\,\sigma^-(t) + i\sqrt{n}. \tag{S31}$$

Therefore, our master equation

$$\dot\rho = -\frac{i}{\hbar}\left[\frac{\Omega}{2}(\sigma^+ + \sigma^-),\rho\right] + \mathcal{L}_L[C_L]\rho + \mathcal{L}_R[C_R]\rho \tag{S32}$$

now includes two Lindblad superoperator terms, where

$$\mathcal{L}_i[C_i]\rho = C_i^- \rho C_i^+ - \frac{1}{2} C_i^+ C_i^- \rho - \frac{1}{2} \rho C_i^+ C_i^- . \tag{S33}$$

We generate the trajectories from Eq. S32 numerically using the Monte Carlo evolution solver in QuTiP (qutip.mcsolve) [8].

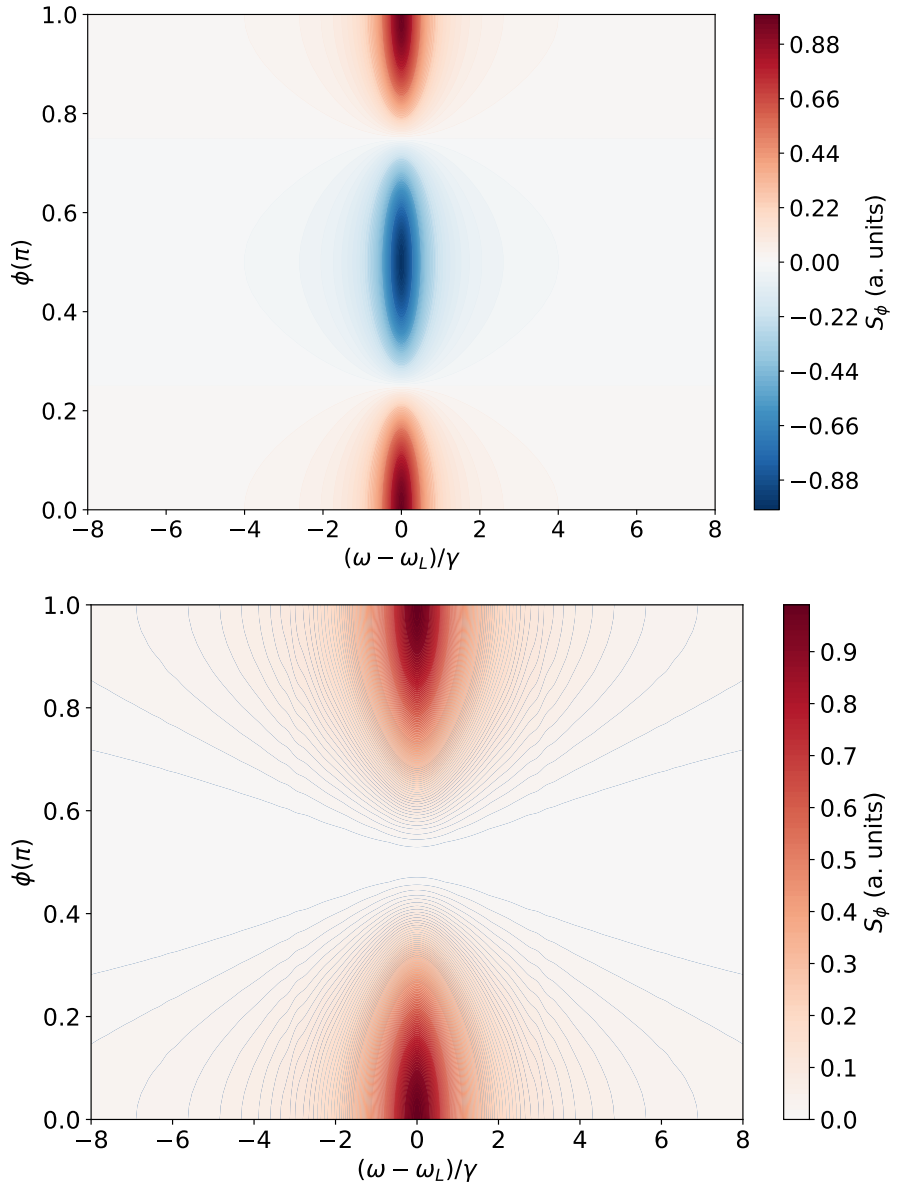

Figure S1: Squeezing example with $\Omega/\gamma = 0.02$, $\Delta = 0$ and $\gamma' = 0$ (top), and $\gamma' = \gamma$ (bottom). The usual in-phase and quadrature-phase positions are $\phi = 0$ and $\phi = \pi/2$, respectively.

Supplementary Note 2 Numerical FDTD Simulations for the Nanowire Quantum Dot Waveguide

Finite difference time domain (FDTD) simulations were used to calculate out-coupling of quantum dot radiation (modeled as a classical dipole) from the nanowire waveguide, and characterize the in-coupling efficiency of a focused Gaussian beam incident on the nanowire under experimental conditions. The geometry of the photonic structure used in the simulations represents a typical nanowire with dimensions shown in Figure 1b of the main text. The nanowire is modeled with a cylindrical base and a conical taper with a full angle of 1.2°. A dielectric with an index of refraction n=3.44 was used to simulate both the nanowire material (Wurtzite InP) and the Zinc Blende InP substrate.

S2.1 Out Coupling Quantum Dot Emission

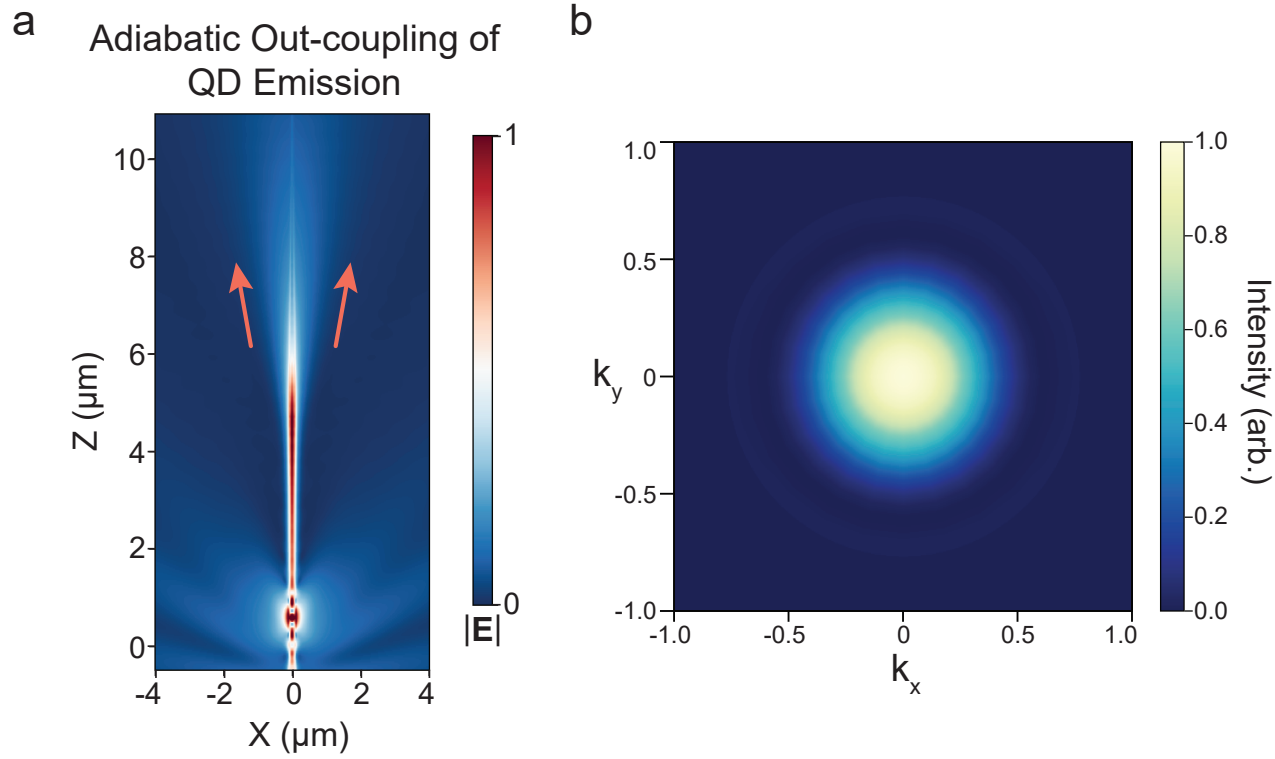

Figure S2: (a) Evolution of the electric field intensity of a radiating dipole coupled to the nanowire waveguide generated via a 3D FDTD simulations. The dipole is located $\sim 1\,\mu$m above the substrate, centered on the axis of the nanowire. The influence of the adiabatic taper is evident at the top part of the nanowire waveguide where the high field intensity inside the waveguide slowly expands from inside the nanowire into free space (indicated by red arrows). (b) Far-field (k-space) distribution of the dipole radiation from the tapered nanowire waveguide system simulation showing a Gaussian emission profile.

S2.2 In-Coupling Gaussian Beam with Mode Matching

The intensity and angular distribution (k-space) of the back-reflected laser field was simulated using FDTD. A Gaussian beam source (fully vectorial) passing through the objective (under the thin lens approximation) was used to simulate the focused laser light. The thin lens was set to have an NA of 0.77, an aperture diameter of 5 mm and an input beam waist of 2.1 mm to mimic experimental conditions. To determine the in-coupling efficiency, a power monitor roughly 600nm x 600nm was placed at the base of the nanowire, which records power of the electromagnetic field inside the nanowire. The focal spot of the Gaussian beam source was varied along the height of the nanowire and the optical power propagating through the nanowire was monitored. It was found that a focal point $\sim 5\mu m$ above the substrate corresponds to the maximum transmission through this power monitor. This focal point was chosen for optimal mode-matching. The electric field intensity distribution recorded on this power monitor under mode-matching conditions can be found in Fig S3b. The fraction of the input electric field intensity coupled into the waveguide mode under optimal mode-matching was calculated to be 97%. For calculating the angular dependence of the back-scattered laser under mode-matched conditions, a box monitor was used that enclosed both the nanowire and the Gaussian beam source, but not the substrate. Note that the bottom facet of the box monitor was disabled to ensure that only the back-reflected light was recorded, and an accurate far-field projection can be computed. The angular dependence of the far-field projection using the box monitor is presented in Fig S3c. The total power propagating through the box monitor (P_b) was used to quantify the backward scattered light intensity. The ratio $E = 1 - (P_{b(NW)}/P_{b(Substrate)})$, where $P_{b(NW)}$ is the intensity of back-scattered light under mode-matching conditions and $P_{b(Substrate)}$ is the back-reflected laser from the substrate in the absence of a nanowire. We find E to be 90% under optimal mode-matching simulations.

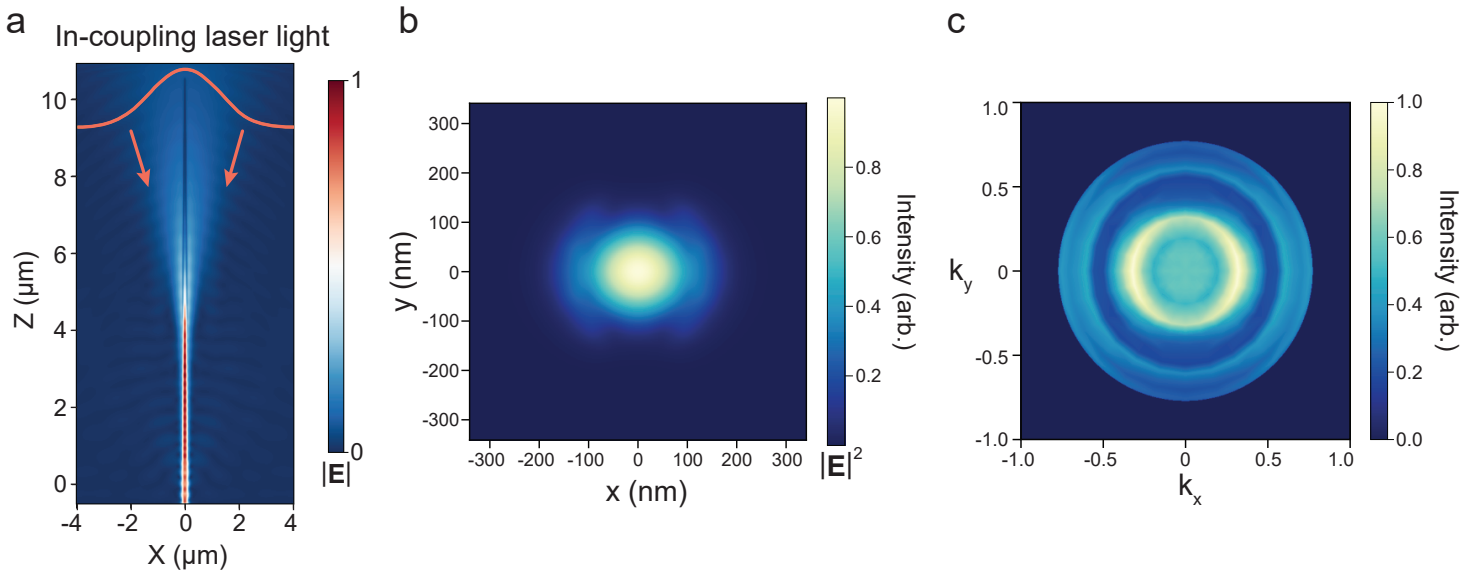

Figure S3: (a) FDTD simulation of a focused Gaussian beam incident on the nanowire waveguide with the an NA matching experimental conditions. (b) Transverse real-space electric field intensity inside the nanowire waveguide under mode-matched input coupling of a Gaussian beam. (c) Simulated far-field scattering distribution in k-space of the back-reflected components from the input Gaussian beam under mode-matched conditions.

Supplementary Note 3 Mode Matching using k-space Imaging

S3.1 Determination of NWQD Output Mode

We use the k-space imaging setup shown in Figure S4 to record the emission mode of the NWQD under above-band excitation, as shown in Fig 2a in the main text. An x-axis line cut of the data was fit to a Gaussian in Figure S5. This fit NA of 0.3 was used to design the optical setup for mode-matching the input laser into the NWQD.

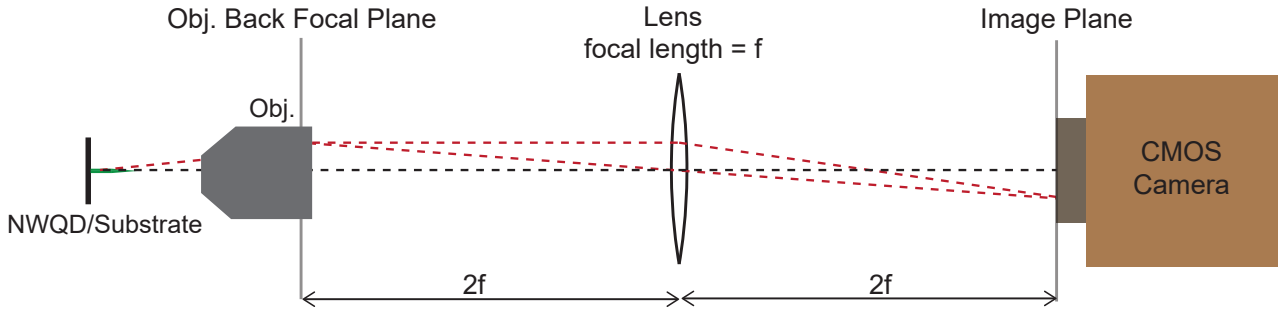

Figure S4: Illustration of the k-space imaging apparatus utilizing a 4-focal length imaging configuration with a high sensitivity CMOS camera.

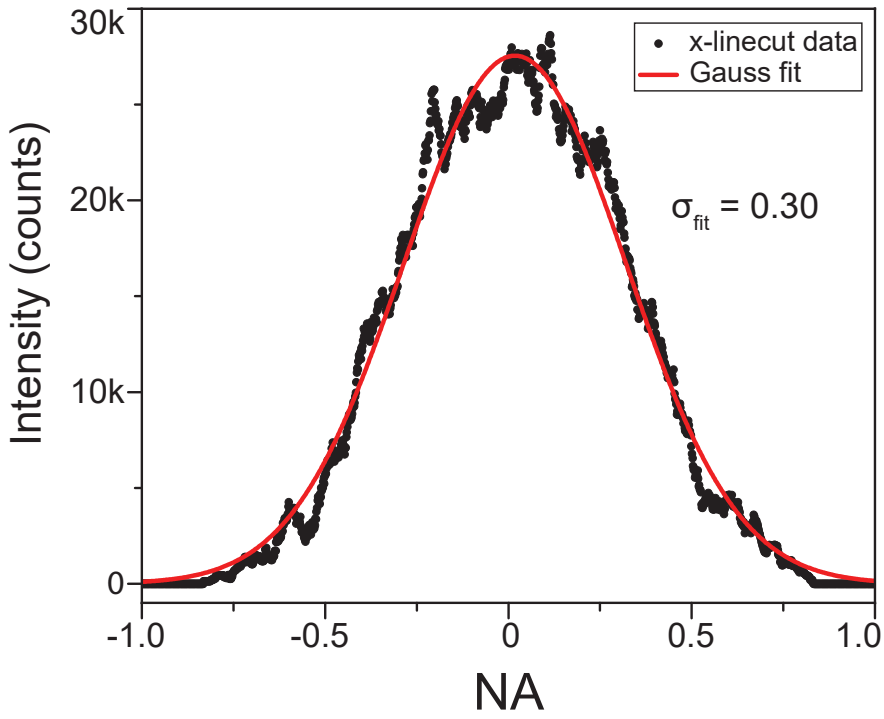

Figure S5: x-linecut of the NWQD emission mode shown in Fig 2a in the main text. A Gaussian fit gives the half-waist at $1/e^2$ to be 0.30 where the R^2 of fit was 0.99.

S3.2 Experimental Mode Matching to NWQD Mode

To determine the correct position of the input beam to achieve ideal mode matching in the experiment, we monitor the scattering of the nanowire in k-space. To begin this process, we roughly park the input laser onto the target nanowire in real space with the laser focused on the substrate. Next, we insert a 4f lens into the optical path for k-space imaging and then retract the objective with a piezo stage in a stepwise manner (1 click = 1 step). In this process, the scattering signal reduces and then we optimize in the lateral directions by further minimizing the scattering singal as seen on a power meter/camera. This process optimization between lateral and vertical locations on the nanowire is iterated until the minimum is obtained in the back scattered intensity. Once at the optimum mode matching position on the nanowire we obtain the k-space image shown in the right panel of Figure 2b in the main text and the mode-matched panel of Figure S4 (fourth from the left on the top). We then systematically move in the lateral direction off the nanowire and obtain the k-space image of the reflected light from the substrate, shown in the left panel of Figure 2b of the main text and the fourth from the left in the bottom panel of Figure S4. Finally, we move back to the optimum mode-matched position on the nanowire and then vary the vertical position along the nanowire. K-space images at various points away from the mode matched condition in both directions is shown in the top panel of Figure S4. As expected, as we move up or down the nanowire, we start to observe a significant increase in the amount of backscattered intensity. In contrast, when off the nanowire, the integrated intensities of the k-space images for various heights away from the substrate show minimal change as seen in the bottom panel of Figure S4. Thus, we systematically confirm that the minimum in back-scattered intensity is our condition for mode matching to the nanowire. We are able to repeatedly perform this procedure on all NWQDs with a single Gaussian mode emission. Extinction values for 10 such nanowires are shown in Table S1.

Table S1: Extinction ratio values of 10 different nanowire quantum dots under mode-matching conditions on the same growth sample.

Nanowire	Extinction ratio
C2 71	0.845
A2 97	0.861
B2 49	0.870
F2 59	0.861
K1 65	0.865
B1 32	0.859
C1 93	0.857
C1 17	0.857
C1 27	0.846
D1 77	0.851
Average:	0.857 ± 0.001

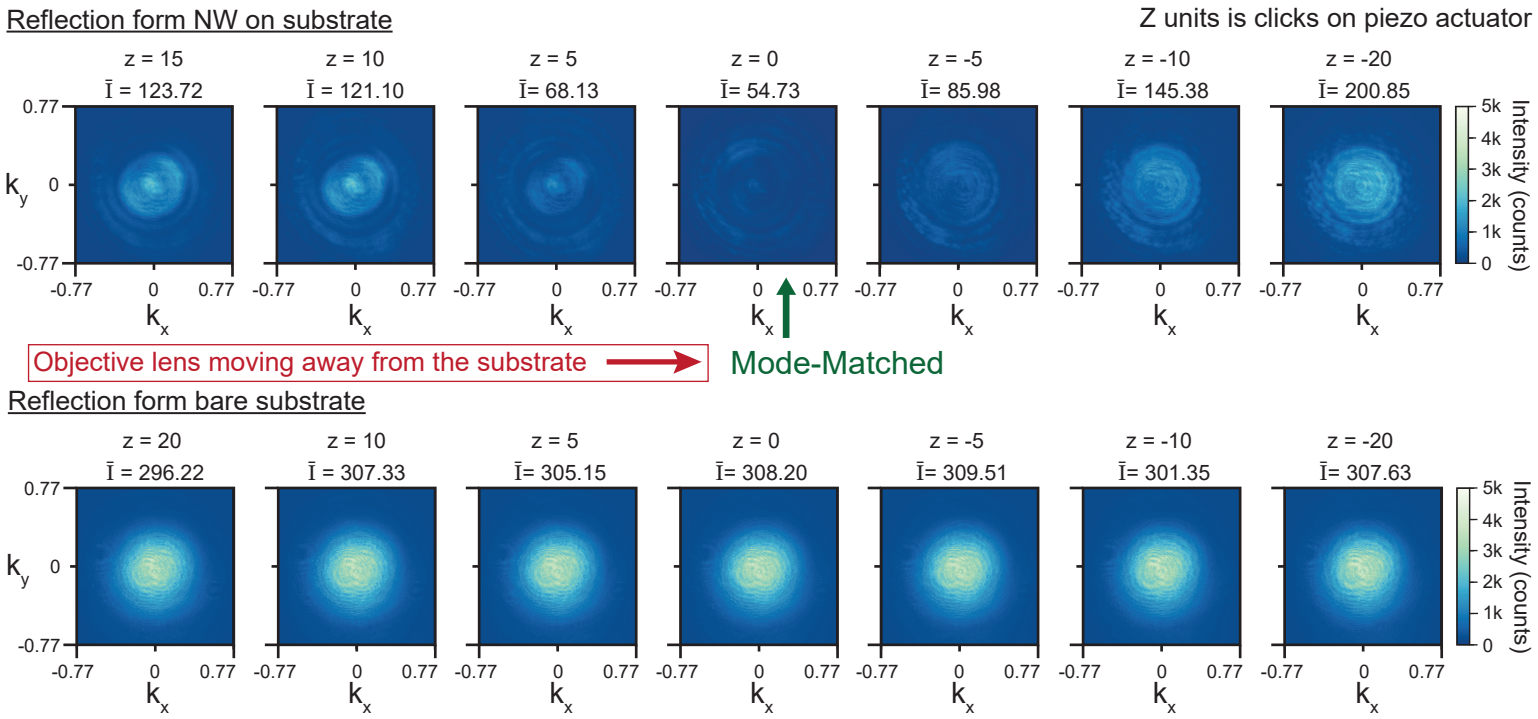

Figure S6: K-Space images of the reflected input laser beam off the nanowire and the flat growth substrate. The gain and exposure time of each image are equal,to ensure that the changes in measured intensity as the z varies are scientifically relevant. Top: K-Space images of the scattering pattern off the nanowire at various focal point locations along the length of the nanowire. Here the input beam is centered laterally on the nanowire. The position $z = 0$ indicates the location where optimal mode matching is achieved. As the z-position is moved from positive to negative, the focal point of the input beam moves away from the substrate. Clearly, at the $z = 0$ mode-matching position, the least amount of intensity is reflected. As the focal position is moved, either above or below the $z = 0$ position, the intensity of back reflection increases while the scattering pattern also changes. Bottom: K-Space images of the laser reflecting from the substrate for the same z-positions. Since the depth of field (twice the Rayleigh length) of the focused input beam is $\sim 5\,\mu$m, the k-space distribution of the laser reflecting from the substrate is invariant along much of the length of the nanowire.

Supplementary Note 4 Estimation of Model Parameters

Objective AR Coated	Windows	Beam Splitter	Dielectric Mirrors	Fiber Coupling Efficiency	Fiber Mating	SNSPD Efficiency	System Total
0.99	$(0.96)^2$	0.93	$(0.995)^4$	0.8	0.9	0.85	0.5

Table S2: Optical transmission efficiency factors for the optical setup used to collect the data in the main text.

Parameter	Value	Description
$T_1 = 1/\gamma_{wg}$	894 ps	Radiative lifetime extracted from the fit in Figure S8.
η_{coll}	0.5	Please see Table S2 for the calculation of the collection efficiency.
η_{in}	0.85	Includes the input coupling efficiency into the NW of 0.95 (see Supplemental Note 2) and the transmission of the objective, windows and a dielectric mirror (number from Table S2 above).
η_{qe}	0.95	Determined from the blinking ratio fitted in Figure S9.
β	0.90	Estimated by comparing FDTD simulations results with our nanowire dimensions obtained using SEM imaging, see Supplementary Note 2.
γ' (HWHM)	0.529 GHz	Extracted from the Lorentzian component of the Voigt fit to the data in Figure 3a of the main text.
σ (STD)	1.87 GHz	Extracted from the Gaussian component of the Voigt fit to the data in Figure 3a of the main text.
b_{frac}	0.001	Extracted from the fit to Figure 3a of the main text. See Equation S9 for the definition of b_{frac}.

Table S3: Summary of parameter values to make the model curves in Figures 3a, 3b and Figure 4a of the main text. A description of how this number was determined is provided in the right-most column.

S4.1 Nanowire Quantum Dot Spectrum

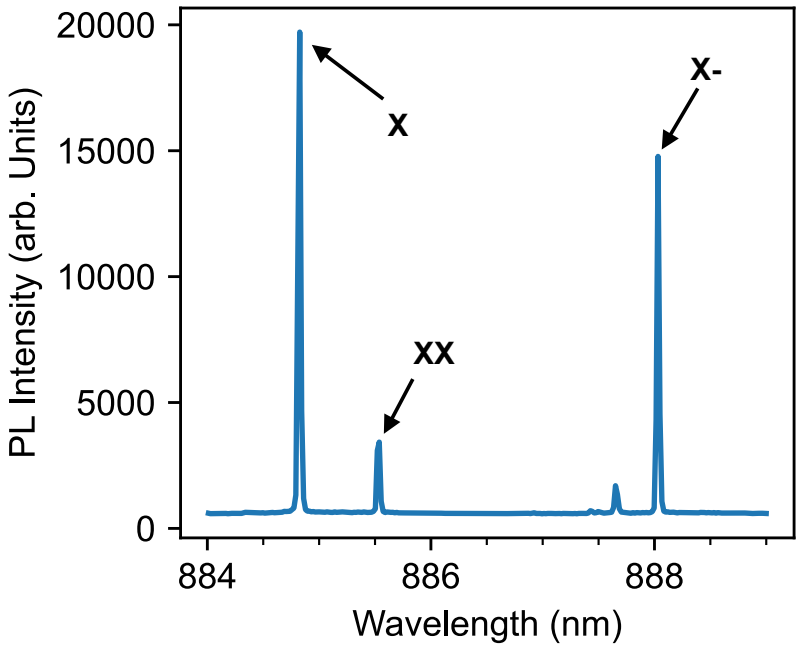

Figure S7: Photoluminescence emission spectrum of the nanowire quantum dot under above bandgap pulsed excitation using a 3ps pulse at 830 nm. The emission lines of the three major exciton complexes (X : neutral exciton, XX : neutral biexciton, X^- : negatively charged exciton) are indicated with arrows.

S4.2 Neutral Exciton Lifetime

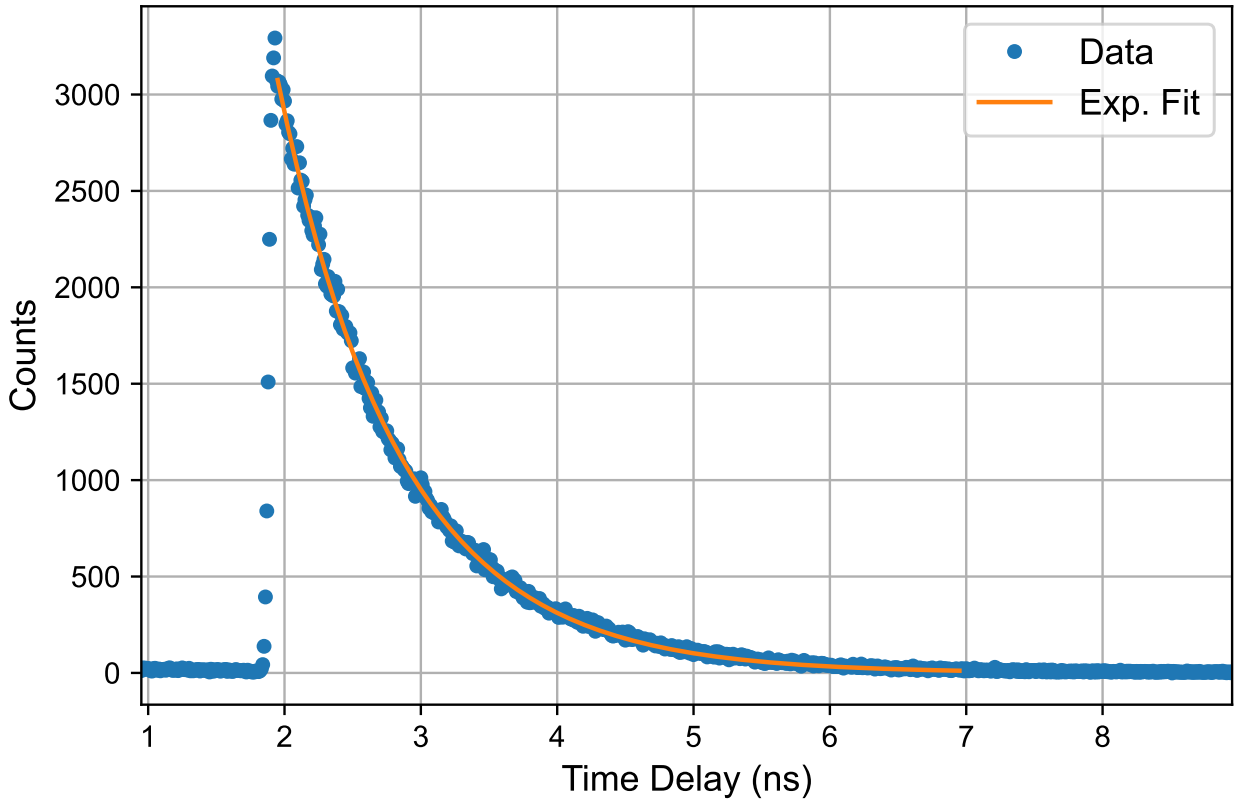

Figure S8: Unpolarized correlation histogram between the neutral biexciton and exciton under 3ps pulsed above bandgap excitation at 830 nm. The exponential decay was fit (yellow) to the data (blue circles) by the function $\exp(-\tau/T_1)$. The 1/e lifetime was found to be $T_1 = 894 \pm 2$ ps.

S4.3 Blinking

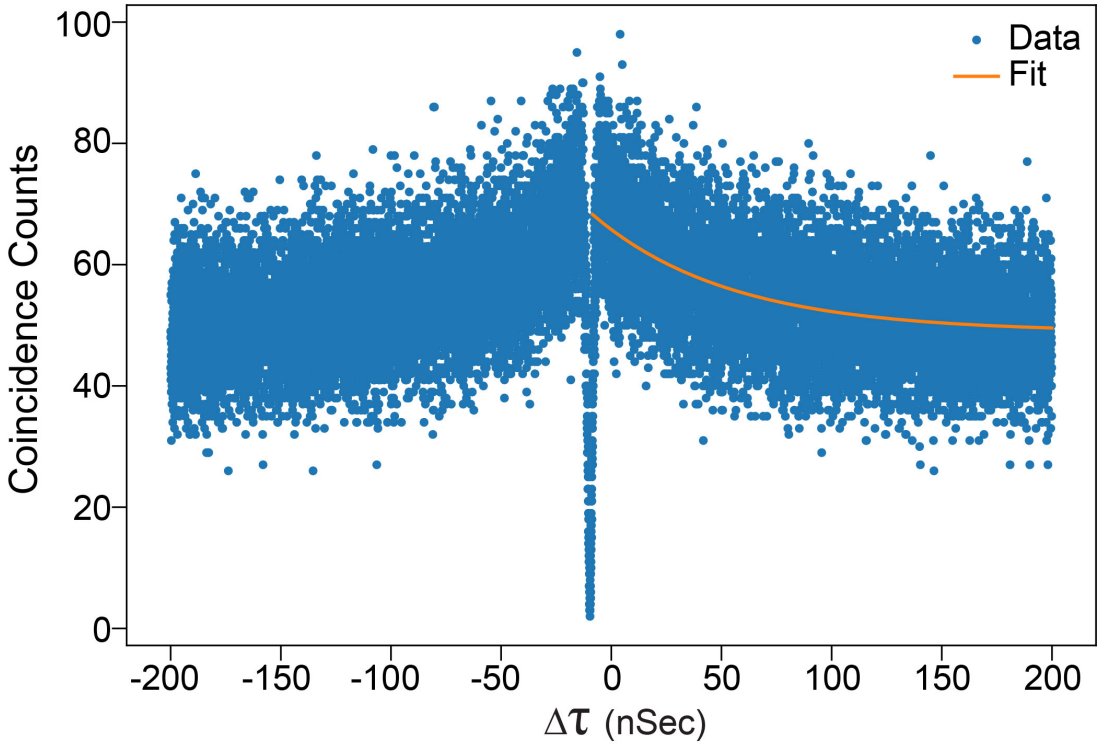

Figure S9: Long delay time trend of the autocorrelation function for $\mu \sim 1e^{-3}$. The fit is to the function: $g^{(2)}_{\text{blink}}(\tau) = 1 + \left(\frac{1-\eta_{qe}}{\eta_{qe}}\right) e^{-\frac{|\tau|}{\tau_c}}$ where 'η_{qe}' is the on-ratio of the dot and τ_c is the characteristic decay time. We find $\eta_{qe} = 0.95$ and $\tau_c = 62\,\text{ns}$. These parameters remain similar over all input drive intensities.

Supplementary Note 5 Effect of Weak Above Band on Resonance Fluorescence

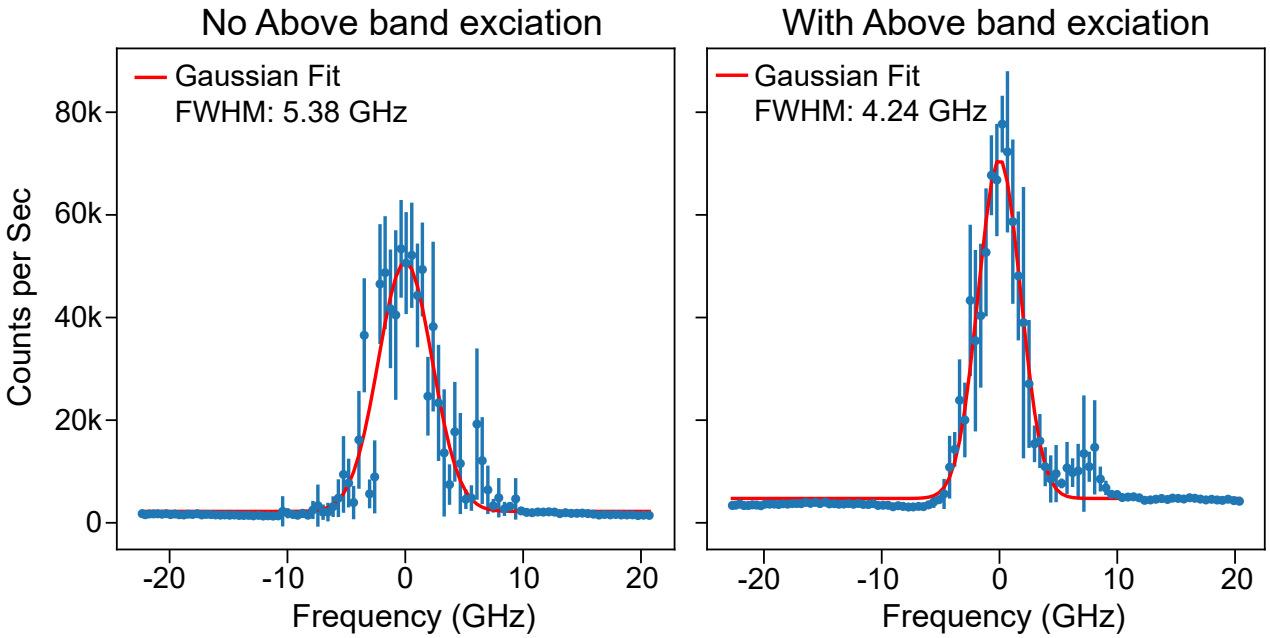

Figure S10: Resonance fluorescence of the NWQD neutral exciton obtained using a narrow (10kHz) CW drive laser scanning across the QD resonance at a power of $\langle n \rangle = 0.01$. Right: A weak CW 830 nm above bandgap laser of 1 pW intensity is sent to the QD in addition to the resonant drive laser. Left: No additional CW 830 nm above bandgap laser is sent to the QD. The presence of the additional above bandgap laser fills some of the charge traps in the vicinity of the QD, thereby reducing the amount of spectral diffusion experienced by the QD [11]. As a result, the Gaussian linewidth of the scan with the weak above bandgap laser (4.2 ± 0.1 GHz) is smaller compared to the one without the weak above bandgap laser (5.4 ± 0.3 GHz).

Supplementary Note 6 Scanning Fabry-Perot Interferometer Response Function

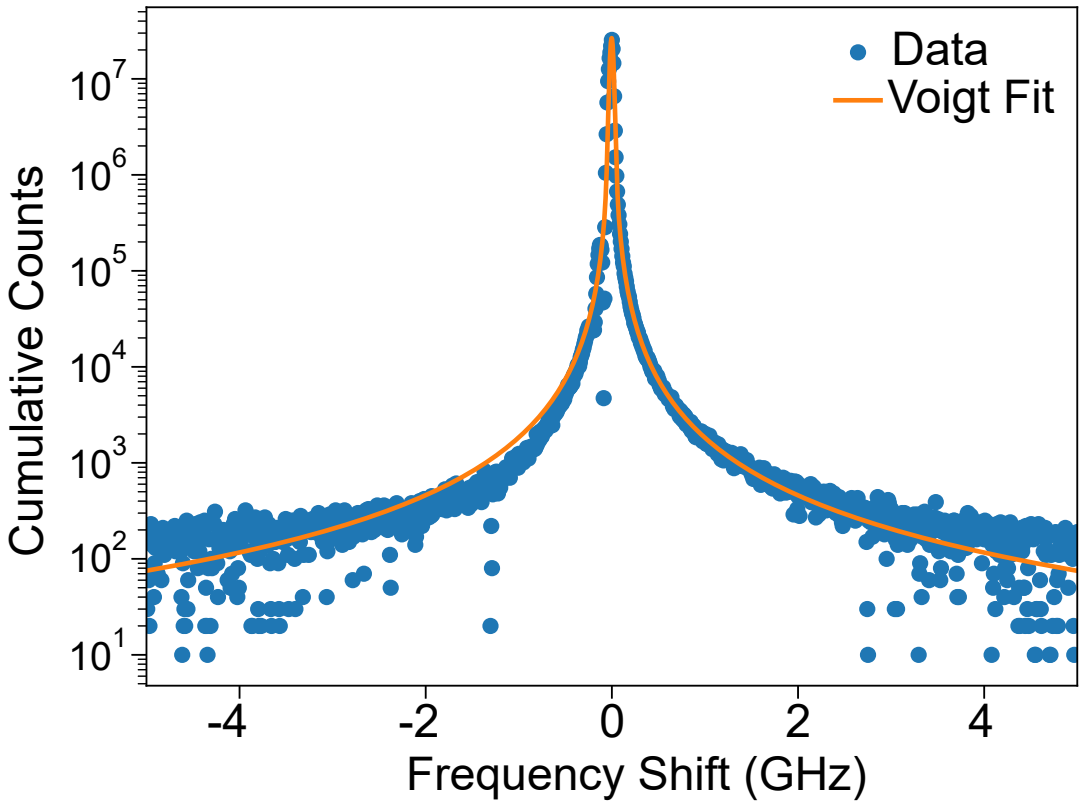

Figure S11: Scan of the narrow laser drive signal through the scanning 10GHz FSR Fabry-Perot interferometer (FPI). The data points (blue) are fit to a Voigt distribution (yellow). The wide frequency response, i.e., tails, of the FPI is dominated by a Lorentzian of FWHM 8 ± 2MHz, whereas the center is dominated by a Gaussian of FWHM 39 ± 5MHz.

References

[1] Shanhui Fan, Şükrü Ekin Kocabaş, and Jung-Tsung Shen. "Input-output formalism for few-photon transport in one-dimensional nanophotonic waveguides coupled to a qubit". In: *Phys. Rev. A* 82.6 (Dec. 2010), p. 063821.

[2] Xin H H Zhang and Harold U Baranger. "Quantum interference and complex photon statistics in waveguide QED". In: *Phys. Rev. A* 97.2 (2018), p. 023813. DOI: 10.1103/PhysRevA.97.023813. URL: http://dx.doi.org/10.1103/PhysRevA.97.023813.

[3] Kevin Lalumière et al. "Input-output theory for waveguide QED with an ensemble of inhomogeneous atoms". In: *Phys. Rev. A* 88 (4 Oct. 2013), p. 043806. DOI: 10.1103/PhysRevA.88.043806. URL: https://link.aps.org/doi/10.1103/PhysRevA.88.043806.

[4] Howard J. Carmichael. *Statistical Methods in Quantum Optics 1*. Springer Berlin Heidelberg, 1999. DOI: 10.1007/978-3-662-03875-8. URL: http://dx.doi.org/10.1007/978-3-662-03875-8.

[5] Howard J Carmichael. *Statistical methods in quantum optics 1: master equations and Fokker-Planck equations*. Springer Science & Business Media, 2013.

[6] Lukas Hanschke et al. "Origin of Antibunching in Resonance Fluorescence". en. In: *Phys. Rev. Lett.* 125.17 (Oct. 2020), p. 170402.

[7] H J Carmichael. "Spectrum of squeezing and photocurrent shot noise: a normally ordered treatment". In: *J. Opt. Soc. Am. B, JOSAB* 4.10 (Oct. 1987), pp. 1588–1603. DOI: 10.1364/JOSAB.4.001588. URL: http://dx.doi.org/10.1364/JOSAB.4.001588.

[8] Neill Lambert et al. "QuTiP 5: The Quantum Toolbox in Python". In: *Physics Reports* 1153 (2026), pp. 1–62. ISSN: 0370-1573. DOI: 10.1016/j.physrep.2025.10.001. URL: https://www.sciencedirect.com/science/article/pii/S0370157325002704.

[9] X T Zou and L Mandel. "Photon-antibunching and sub-Poissonian photon statistics". In: *Phys. Rev. A* 41.1 (Jan. 1990), pp. 475–476. DOI: 10.1103/physreva.41.475. URL: http://dx.doi.org/10.1103/PhysRevA.41.475.

[10] H J Kimble, M Dagenais, and L Mandel. "Photon Antibunching in Resonance Fluorescence". In: *Phys. Rev. Lett.* 39.11 (Sept. 1977), p. 691. DOI: 10.1103/PhysRevLett.39.691. URL: http://dx.doi.org/10.1103/PhysRevLett.39.691.

[11] Jingzhong Yang et al. "Photoneutralization of charges in GaAs quantum dot based entangled photon emitters". In: *Phys. Rev. B.* 105.11 (Mar. 2022), p. 115301. DOI: 10.1103/physrevb.105.115301. URL: https://link.aps.org/doi/10.1103/PhysRevB.105.115301.